

# Polycrystal model of the mechanical behavior of a Mo–TiC<sub>30 vol.%</sub> metal–ceramic composite using a three-dimensional microstructure map obtained by dual beam focused ion beam scanning electron microscopy

D. Cédât<sup>a</sup>, O. Fandeur<sup>b</sup>, C. Rey<sup>a,\*</sup>, D. Raabe<sup>c</sup>

<sup>a</sup> *Departement Mechanical Soils, Structures and Materials, Ecole Centrale Paris, F-92295 Châtenay-Malabry, France*

<sup>b</sup> *CEA, DEN, DM2S, SEMT, LM2S, F-91191 Gif-sur-Yvette, France*

<sup>c</sup> *Department Microstructure Physics and Metal Forming, Max Planck Institut für Eisenforschung, Düsseldorf, Germany*

Received 16 July 2011; received in revised form 25 November 2011; accepted 27 November 2011

## Abstract

The mechanical behavior of a Mo–TiC<sub>30 vol.%</sub> ceramic–metal composite was investigated over a wide temperature range (25–700 °C). High-energy X-ray tomography was used to reveal percolation of the hard titanium carbide phase through the composite. Using a polycrystal approach for a two-phase material, finite-element simulations were performed on a real three-dimensional (3-D) aggregate of the material. The 3-D microstructure, used as the starting configuration for the predictions, was obtained by serial sectioning in a dual beam focused ion beam scanning electron microscope coupled to an electron backscattered diffraction system. The 3-D aggregate consists of a molybdenum matrix and a percolating TiC skeleton. As for most body-centered cubic (bcc) metals, the molybdenum matrix phase is characterized by a change in plasticity mechanism with temperature. We used a polycrystal model for bcc materials which was extended to two phases (TiC and Mo). The model parameters of the matrix were determined from experiments on pure molybdenum. For all temperatures investigated the TiC particles were considered to be brittle. Gradual damage to the TiC particles was treated, based on an accumulative failure law that is approximated by evolution of the apparent particle elastic stiffness. The model enabled us to determine the evolution of the local mechanical fields with deformation and temperature. We showed that a 3-D aggregate representing the actual microstructure of the composite is required to understand the local and global mechanical properties of the composite studied.

© 2011 Acta Materialia Inc. Published by Elsevier Ltd. All rights reserved.

**Keywords:** Metal–ceramic composite; Numerical simulation; Crystal plasticity; Polycrystal modeling; Damage

## 1. Introduction

The aim of this study was to understand the mechanical behavior and damage evolution of a metal–ceramic composite (Mo–TiC<sub>30 vol.%</sub>) as a function of deformation and temperature in the range 800 °C up to 1000 °C.

For compression tests performed at high temperature damage observations cannot be monitored and simulations

are needed at the grain scale, to obtain a better understanding of damage initiation.

In an earlier study Cédât et al. [4] simulated the local mechanical fields using a three-dimensional (3-D) aggregate obtained from a random stack of layers of columnar grains. These grains were characterized in terms of crystal orientations, determined by electron backscattered diffraction (EBSD). When using this aggregate the polycrystal model failed to describe the mechanical behavior of the composite. Different effects might be responsible for the discrepancy between experiment and predictions, namely microstructural size effects, higher complexity of the

\* Corresponding author.

E-mail address: [colette.rey@ecp.fr](mailto:colette.rey@ecp.fr) (C. Rey).

required constitutive laws of the phases involved, and the spatial distribution (connectivity and topology) of the TiC brittle phase.

The current paper addresses this problem of properly predicting the micromechanical behavior of complex metal–ceramic composites.

The investigations in Section 2 (using tomography) reveal percolation of the TiC phase. A new representative aggregate has been built to take into account such phase percolation in the computation of the local mechanical fields, using tomographic microstructure data obtained by dual beam focused ion beam scanning electron microscopy (FIB-SEM).

The polycrystal model used, implemented in finite-element code, is described in Section 3. Damage is represented by a decrease in the TiC effective elastic modulus implemented in the model.

Section 4 presents the meshing and the boundary conditions applied to the 3-D EBSD aggregate. New model parameters for Mo are determined by an inverse method. Section 5 deals with the results of the mechanical predictions for the composite. Section 6 draws conclusions.

## 2. Material and experimental procedures

The material investigated was obtained by powder metallurgy synthesis [2,3] (hot isostatic pressing (HIP) at 1600 °C). No homogenization heat treatment was performed after HIP processing.

The composite microstructure was characterized in a previous paper [4] using different chemical and physical methods. According to Cédât et al. [1] the composite exhibited three phases: molybdenum (Mo), titanium carbide (TiC) and a (Mo,Ti) C phase, which is a face-centered cubic (fcc) structure with lattice parameters close to those of TiC (Fig. 1). The hard particles (TiC) showed a core/shell (or core/rim) structure, with molybdenum as the binder phase. The third phase, identified as TiC–Mo<sub>15</sub> at.%, had the same structure as TiC. In this paper the mechanical behavior of the third phase is assumed to be equivalent to that of TiC.

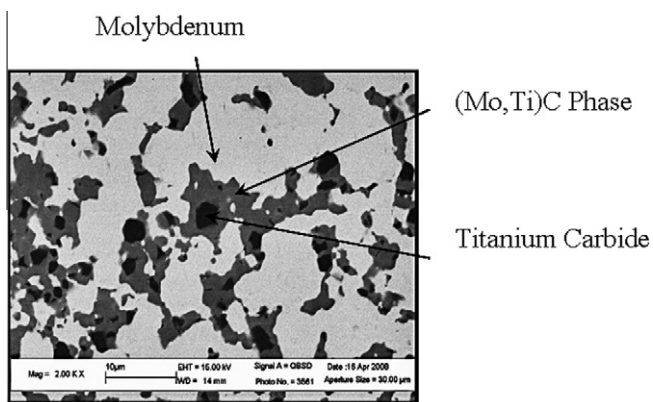


Fig. 1. SEM picture showing the microstructure of the Mo–TiC<sub>30</sub> vol.% composite revealing three phases, molybdenum (light grey), TiC (black), and (Mo,Ti) C (grey) [1].

### 2.1. Chemical composition

The chemical compositions of the powder are given in Tables 1 and 2.

### 2.2. X-ray tomography results

Using high-energy X-ray tomography a 3-D investigation of the material was performed at the European Synchrotron Radiation Facility (ESRF, Grenoble, France). This characterization technique proceeds by taking a sequence of recordings of a sample from different angles. Then an appropriate tomography reconstruction algorithm builds a 3-D map of the microstructure based on inversion of the X-ray attenuation coefficient projection paths that penetrated the material upon synchrotron illumination. Fig. 2 shows a 3-D image of the microstructure of the Mo–TiC material obtained with the highest spatial resolution (0.28 μm) available on the ID19 beam line (X-ray energy 65 keV) of the ESRF equipment.

Fig. 2 represents the set of all points in the carbide phase (purple) that can be linked together to the bottom and top faces of the parallelepiped specimen (30 × 30 × 30 μm), by paths entirely contained in the carbide phase. The microstructure of the composite revealed a percolating skeleton of carbides embedded in a molybdenum metallic matrix, with a high 3-D connectivity of the carbide phase.

### 2.3. 3-D aggregate mapping by 3-D EBSD

To accurately compute the local mechanical fields a new representative 3-D aggregate had to be designed, taking into account the observed percolation of the TiC phase. Our approach to 3-D EBSD was inspired by the works of Uchic et al. [5], Zaefferer et al. [6], Bastos et al. [7] and Konrad et al. [8], as well as by the 3-D texture measurements using synchrotron radiation published by Larson et al. [9] and Yang et al. [10]. The 3-D EBSD experiments were conducted at the Max-Planck Institute (Düsseldorf), using a joint high-resolution field emission SEM/EBSD set-up together with a FIB system in the form of a Zeiss cross-beam 3-D crystal orientation microscope. Details are given in Larson et al. [9] and Yang et al. [10].

The analytical method applied in this study involves highly precise and fully automated serial sectioning by Ga<sup>+</sup> FIB and subsequent mapping of the crystallographic texture in each of those layers using high-resolution EBSD. For more details on this method, see Zaafarani et al. [11] and Zaefferer et al. [12].

The spatial resolution of the 3-D orientation and phase pixel information retrieved amounts to 50 × 50 × 50 nm. The ion beam did not create noticeable damage, i.e. no serious deterioration of the EBSD pattern quality could be observed after milling. This stability of the material when exposed to an ion beam is attributed to its high melting point and the absence of phase transformations. The EBSD measurements were carried out sequentially in each layer

Table 1  
TiC composition (mass%).

C	O	N	Ca	Co	W	Ni	Al	Fe	S
19.23	0.6126	0.0279	0.002	0.032	0.39	<4E-4	0.0014	0.0061	0.0019

Table 2  
Molybdenum composition (mass%).

Mo	O	Fe	K
99.98	0.0620	9 p.p.m.	29 p.p.m.

after FIB serial sectioning at a 300 nm step size between the abutting layers. The entire process of alternating FIB sectioning and EBSD measurements was carried out for a set of 22 layers to reconstruct the whole aggregate. Fig. 3 shows SEM images of two different serial sections and the entire 3-D microstructure reconstructed as a 3-D map.

2.4. Experimental analysis of the mechanical behavior of the composite and of the molybdenum phase

2.4.1. Composite

The composite compression curves are given in Fig. 4 for temperatures between 25 °C and 700 °C. The specimen

are cylinders with a diameter  $D = 12$  mm and cylinder length  $L = 18$  mm. The initial strain rate upon loading was about  $\dot{\epsilon} = 5 \times 10^{-4} \text{ s}^{-1}$ .

The compression curves show a linear elastic stage, followed by a linear hardening stage, and, finally, a weak strain hardening regime. The two strain hardening regimes change as a function of temperature and deformation. The extension of the linear stage decreases with increasing total deformation. Strain hardening decays with increasing temperature.

Fracture surface observations reveal that at 25 °C the two phases are characterized by a brittle behavior and that at 300 °C the molybdenum matrix is ductile while the TiC phase fails in a brittle manner. The mechanical properties of pure molybdenum have been previously studied by Cédât et al. [1] using two kinds of tensile tests, namely strain rate change tests ( $5 \times 10^{-4}$  and  $5 \times 10^{-2} \text{ s}^{-1}$ ) over

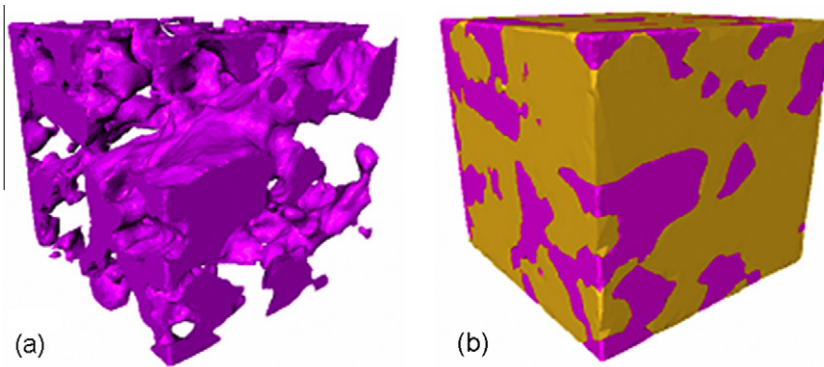


Fig. 2. 3-D representation of the phases obtained by X-ray tomography. (a) TiC; (b) Mo composite. Specimen size  $30 \times 30 \times 30 \mu\text{m}$ .

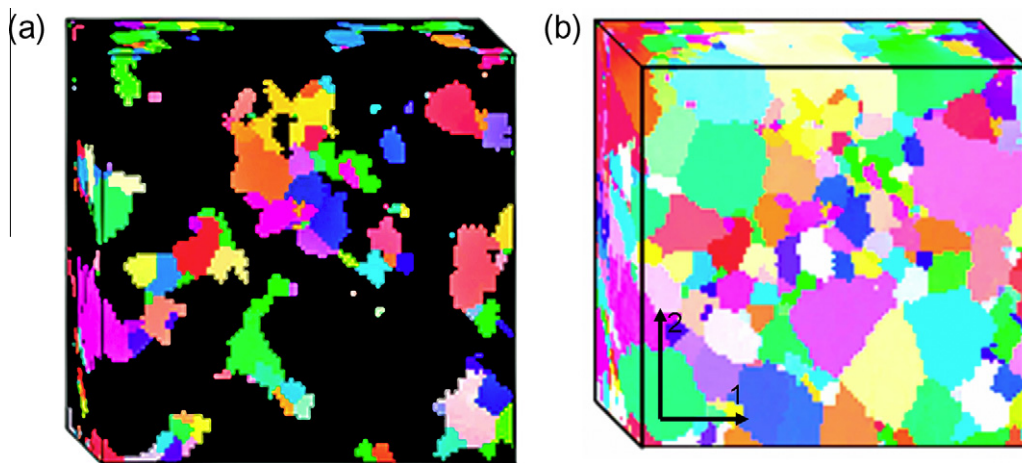


Fig. 3.  $30 \times 30 \times 6.6 \mu\text{m}$  aggregate obtained by 3-D electron orientation microscopy (3D EBSD). Top row, TiC and TiC–Mo<sub>15</sub> at.% phases; bottom row, whole aggregate. The color code is given by the crystallographic standard triangle. For simulations the loading direction is parallel to the  $\vec{2}$  axis. (For interpretation of the references to colour in this figure legend, the reader is referred to the web version of this article.)

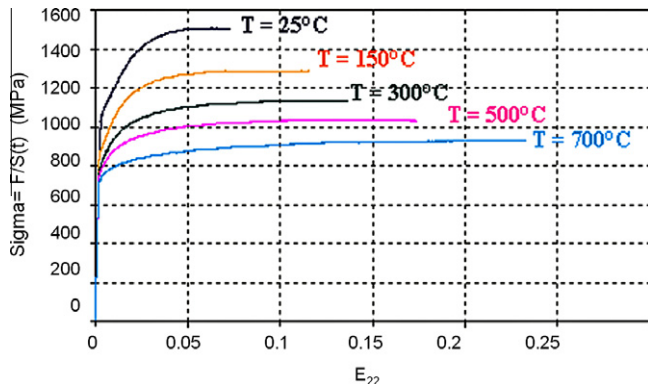


Fig. 4. Experimental composite compression behavior tests.  $\sigma$ , tensile stress;  $F$ , force;  $S(t)$ , cross-section at each time interval;  $E_{22}$ , strain.

the temperature range 25–700 °C and temperature change tests. A transition in the polycrystal mechanical mechanisms was observed above 150 °C. For  $T > 300$  °C the viscoplastic flow weakly varied with temperature. These results, confirmed by transmission electron microscopy (TEM) observations, suggested that molybdenum—like most body-centered cubic (bcc) metals—reveals different plasticity properties at low and high temperatures. In bcc transition metals screw dislocations are less mobile than edge dislocations. Screw dislocation motion proceeds via thermally activated kink pair formation and expansion. Optical microscopy (OM) and SEM observations [13] performed on molybdenum surfaces as well as on fracture surfaces after tensile testing confirmed these results. For  $T = 25$  °C molybdenum rupture occurs by grain boundary decohesion. The fracture surfaces studied reveal features of brittle failure. For  $T = 200$  °C grain boundary decohesion and plastic glide is observed. For  $T = 300$  °C deformation occurs by plastic glide and the fracture surface is characterized by ductile rupture features.

From these observations we concluded in our earlier work that the plasticity mechanisms of this material change in the temperature range around 200 °C. One should note that this transition temperature  $T_0$  is different from the brittle to ductile transition temperature of molybdenum (which is close to 25 °C).

### 3. Polycrystal model

In order to determine the local mechanical fields in the different phases and especially the location and origin of damage in the TiC phase a previous model [14] was upgraded and numerical simulations were conducted. The crystal plasticity model used was developed within the framework of large transformations [15–20] (small elastic distortion but large lattice rotation) and was implemented in the Abaqus finite-element code, using a UMAT user subroutine.

The polycrystal is composed of different grains, each one having its own size and crystallographic orientation. Each grain is considered as a single crystal characterized by a constitutive law presented below.

This polycrystal model was developed for bcc metals or alloys taking into account temperature effects, as will be outlined in more detail below. The two plasticity mechanisms controlling plastic strain hardening of molybdenum are double kink formation (low temperature) and interactions between mobile and forest dislocations (high temperature). In this paper we summarize the polycrystal model extended to multi-phase composites. For more details see Libert [18] and Libert et al. [14].

#### 3.1. Single crystal constitutive law for the molybdenum matrix

For the bcc crystal structure of the molybdenum matrix plastic glide occurs on the 24 slip systems  $\{110\}\langle 111\rangle$  and  $\{112\}\langle 111\rangle$ . The chosen viscoplastic law can describe the competition between lattice friction and forest hardening. According to Kubin et al. [21], Rauch [22] and Tabourot et al. [23] the slip rate on a given slip system (hereafter referred to by the index  $s$ ) is given by:

$$\dot{\gamma}^s = \dot{\gamma}_0 \exp \left[ -\frac{\Delta G(\tau_{\text{eff}}^s)}{kT} \right] \text{sgn}(\tau^s) \quad (1)$$

where  $\Delta G(\tau_{\text{eff}}^s)$  is the energy of activation for crystallographic slip of lattice dislocations, which is a function of the effective shear stress  $\tau_{\text{eff}}^s$ .  $\tau^s$  and  $\dot{\gamma}_0$  are the resolved shear stress on system  $s$  and the reference shear rate, respectively.

When  $T < T_0$  the shear rate  $\dot{\gamma}_0$  depends on the geometry of the segments of the screw dislocations. The energy of activation is then associated with the double kink mechanism and is given by a phenomenological description, as proposed by Kocks et al. [24]:

$$\Delta G(\tau_{\text{eff}}^s) = \Delta G_0 \left( 1 - \left( \frac{|\tau_{\text{eff}}^s|}{\tau_R} \right)^p \right)^q \quad (2)$$

where  $p$  and  $q$  are parameters describing the energy associated with the Peierls barrier. In Eq. (2)  $\tau_R$  is the effective stress that is required to create a double kink at  $T = 0$  K, when the contribution of thermal activation is equal to zero. This description assumes that the glide of dislocations on a system  $s$  is activated when  $\tau_{\text{eff}}^s$  is larger than  $\tau_R$ .

#### 3.2. Single crystal strain hardening law for the molybdenum matrix

Strain hardening evolution as a function of temperature depends on interactions between mobile dislocations with lattice friction and/or forest dislocations. Lattice friction generates short-range stresses described by the effective stress  $\tau_{\text{eff}}^s$ . The contributions described by  $\tau_{\text{int}}^s$  and  $\tau_0$  are shear stresses and represent the interaction between mobile and latent dislocations. Thus the yield stress required to activate the glide system  $s$  is equal to the sum of the three contributions:

$$\tau^s = \tau_0 + \tau_{\text{eff}}^s + \tau_{\text{int}}^s \quad (3)$$

Considering a segment of a screw dislocation pinned by two obstacles submitted to lattice friction  $\tau_0$ , Rauch [22] proposed the following expression of the internal stress:

$$\tau_{\text{int}}^s = \frac{(\mu b)^2 \sum_{u=1,24} a^{\text{su}} \rho^u}{\tau^s - \tau_0} \quad (4)$$

where  $a^{\text{su}}$  is a component of the dislocation interaction matrix as proposed by Franciosi [25], which is due to the interaction strength between the slip systems  $s$  and  $u$  (self and latent hardening). Latent hardening experiments [25], performed on single crystals under tensile testing, revealed that the  $a^{\text{su}}$  parameter depends on the strain value: they increase up to 0.5–1% straining, then reaches asymptotic values. In this paper we use the asymptotic values.  $\rho^u$  is the dislocation density on the glide system  $u$ . Merging Eqs. (3) and (4) and solving the resulting equation one obtains:

$$\tau^s = \tau_0 + \frac{\tau_{\text{eff}}^s}{2} + \frac{1}{2} \sqrt{(\tau_{\text{eff}}^s)^2 + 4(\mu b)^2 \sum_u a^{\text{su}} \rho^u} \quad (5)$$

The general expression of the hardening law (Eq. (5)) is appropriate to describe continuous evolution of the shear stress as a function of temperature:

In the case of low temperature behavior ( $T < T_0$ ) plasticity is governed by the reduced mobility of screw dislocations and the double kink mechanism, hence  $\tau_{\text{int}}$  is negligible compared with  $\tau_{\text{eff}}$ . Eq. (5) leads to:

$$\tau^s = \tau_{\text{eff}}^s + \frac{(\mu b)^2 \sum_{u=1,24} a^{\text{su}} \rho^u}{\tau_{\text{eff}}^u} \quad (6)$$

In the case of high temperature ( $T > T_0$ ) plasticity mainly depends on forest hardening and  $\tau_{\text{eff}}$  is negligible compared with the two other terms. Eq. (5) leads to:

$$\tau^s = \tau_0^s + \mu b \sqrt{\sum_{u=1,24} a^{\text{su}} \rho^u} \quad (7)$$

At low temperatures plastic deformation occurs according to two non-equivalent slip system families  $\langle 111 \rangle \{110\}$  and  $\langle 111 \rangle \{112\}$ .

### 3.3. Dislocation density evolution law

The dislocation density evolution law is a generalization of the relation proposed by Estrin and Mecking [26]. For each slip system Eq. (8) describes the evolution of the 24 dislocation densities with the strain:

$$\dot{\rho}^s = \frac{|\dot{\gamma}^s|}{b} \left[ \frac{1}{D_{\text{grain}}} + \frac{\sqrt{\sum_{u \neq s} \rho^u}}{K(T)} - g_c(T) \rho^s \right] \quad (8)$$

This expression is derived from the balance between dislocation accumulation (Orowan's relationship) and dislocation annihilation which induces softening.  $K(T)/\sqrt{\sum_{u \neq s} \rho^u}$  is the dislocation mean free path, which increases with decreasing temperature. As evolution of the dislocation density is weak at low temperature, we assume that  $K(T)$  increases with decreasing temperature. The annihilation of dislocations is controlled by the mean dislocation–dislocation spacing  $g_c$ , the temperature dependence of which is expressed here in terms of an Arrhenius law:

$$g_c(T) = g_{c0} \exp \left[ -\frac{E_{gc}}{k_B(T)} \right] \quad (9)$$

According to Eq. (9) two dislocations of the same system  $s$  may undergo annihilation as soon as they are separated by a spacing below  $g_c$ . Similar dislocation-based constitutive laws for crystal plasticity finite-element models were applied, as suggested by Ma et al. [17,27].

### 3.4. Damage law for the titanium carbide particles

Damage in the compound starts by initiation of cracks within the brittle carbide phase. A simple criterion that rests on the local stress in the brittle phase is introduced in the polycrystal model. The failure strength of ceramics under compression being approximately 10–15 times larger than the tensile strength [28], the critical stress leading to damage initiation is given by the approximation:

$$\sigma_c = \sigma_{\text{tensile}} \approx \frac{\sigma_{\text{compressive}}}{15} \quad \text{with} \quad \sigma_{\text{tensile}} = \frac{K_{\text{IC}}}{\sqrt{\pi a}} \quad (10)$$

where  $K_{\text{IC}}$  is the toughness factor and  $a$  the mean size of the crack.

The results of the simulations show that the carbide phase is mainly under tension when the composite is mechanically loaded, while the molybdenum phase is under compression. For the carbide phase the chosen damage criterion is formulated as a measure of the gradual accumulation of damage. It is based on evolution of the elastic law:

$$\tilde{C}(t) = \tilde{C}_0 [1 - D(t)] \quad (11)$$

with

$$D(t) = \frac{\beta}{\alpha} [1 - \exp(-\alpha(t - t_0))] \quad (12)$$

where  $t - t_0 = \varepsilon/\dot{\varepsilon}$ , and  $\varepsilon$  and  $\dot{\varepsilon}$  are the local strain and local strain rate at a given point, respectively.  $\tilde{C}_0$  is the initial elastic modulus tensor and  $\tilde{C}(t)$  is “the effective modulus”, which gradually decays as a function of the strain rate and the strain.  $\alpha$  and  $\beta$  are parameters that are arbitrarily chosen in order to create an abrupt decrease in the Young's modulus due to micro-crack formation. A positive critical stress value  $\sigma_c$  is determined from (Eq. (10)). At each increment of the simulation the criterion (Eq. (10)) is tested for all elements of the TiC meshing. As soon as the criterion  $\sigma \geq \sigma_c$  ( $\sigma$  is the local equivalent stress) is verified within an element its effective modulus is decreased as given by Eqs. (11) and (12). For  $D(t) = 1$  ( $C(t) = 0$ ) the element is equivalent to a “hole”. Changes in the stiffness of some elements of the TiC phase contribute to that of the overall compound.

## 4. Boundary conditions, meshing and model parameters

The polycrystal model was implemented in Abaqus™ finite-element code using an UMAT subroutine. Most of the molybdenum parameters are determined on the basis of the experimental curves, using an inverse fitting method using coupling [18,20] between the Sidolo™ and Abaqus™ software packages. The initial density of the dislocations

before straining was determined by TEM. The parameters used for molybdenum are given in Tables 3 and 4.

#### 4.1. The aggregate

The polycrystalline aggregate is shown in Fig. 3. The finite-element meshing is derived from the grid corresponding to the 3-D EBSD (0.3  $\mu\text{m}$  step) measurements. It is built from 220,000 elements (C3D8R). Each element corresponds to an original 0.3  $\mu\text{m}$  square pixel of the material.

The crystallographic microstructural properties of the two phases are described in terms of the Euler angles for each pixel of the two phases in the mesh, the TiC elastic properties, and the molybdenum constitutive laws parameters. Connectivity among the two phase sets and the percolation of TiC are thus automatically taken into account.

#### 4.2. Boundary conditions

The aggregate considered corresponds to one-eighth of the whole computed structure. For symmetry reasons the lower face of the crystalline aggregate, shown in Fig. 3, is loaded in compression mode normal to direction  $\vec{2}$ . The displacement is  $u_2 = 0$  on the lower face. The other boundary conditions are  $u_3 = 0$  on the face normal to the  $\vec{3}$  direction and the parallel surface is free. The  $u_2$  applied displacement corresponds to a strain rate of about  $5 \times 10^{-4} \text{ s}^{-1}$ .

In addition to this set of parameters, this new investigation has identified temperature-dependent parameters by an inverse method on the basis of experimental tensile curves performed at 25–700 °C.

The titanium carbide elasticity is assumed to be isotropic. Its features are given in Table 5.

According to our observations of the fracture surfaces we assume perfect cohesion between TiC and the Mo matrix.

## 5. Results and discussion

For pure molybdenum metal representing a polycrystal matrix the simulation results delivered by the current polycrystal model have already been published [4]. The compression test simulations were in good agreement with the experimental results.

#### 5.1. Mo–TiC composite results for $T = 25^\circ\text{C}$

The numerical and experimental curves are compared in Fig. 5.

At room temperature very good agreement is observed between the numerical (Fig. 5) and experimental (Fig. 4)

Table 4  
Set of temperature-dependant parameters identified for molybdenum.

$T$	$\Delta G(T)$ (eV)	$\tau_0$ (MPa)	$K$	$g_c$ (nm)
25 °C	0.35	125	440	20
150 °C	0.5	70	80	12
300 °C	0.97	70	50	26
500 °C	1.18	70	50	30
700 °C		70	30	36

$\tau_0$ , shear stress due to lattice friction (Eq. (3));  $\Delta G(T) = \Delta G(\tau_{\text{eff}})$ , slip systems energy of activation (Eq. (1));  $K(T)$ , material parameter associated with the dislocation mean free path (Eq. (8));  $g_c$ , dislocation–dislocation annihilation distance (Eqs. (8) and (9)).

Table 5  
Parameters for titanium carbide (TiC) derived from the proposed model.

$E$ (GPa)	$\nu$	$\alpha$	$\beta$	$\sigma_c$ (MPa)
440	0.19	0.013	0.013	250

$E$ , Young's modulus;  $\nu$ , Poisson coefficient;  $\sigma_c$ , rupture critical parameter in tension.

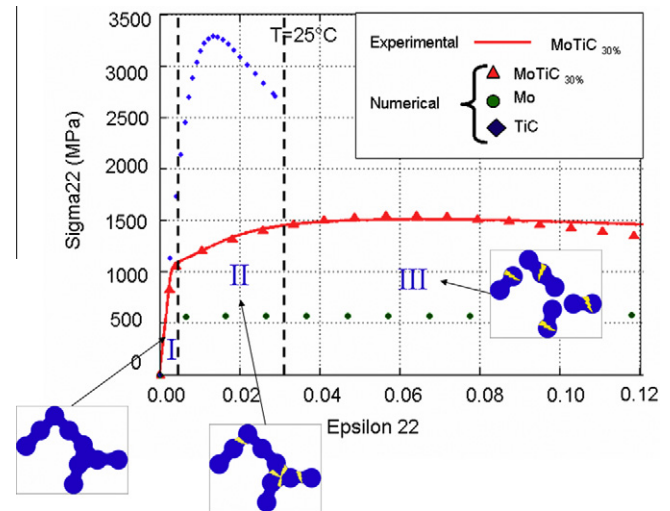


Fig. 5. Numerical and experimental compression curves for Mo, TiC and Mo–TiC<sub>30</sub> vol.% ( $T = 25^\circ\text{C}$ ).  $\sigma_{22}$ , compression stress;  $\epsilon_{22}$ , strain.

curves, up to the maximum stress. Compared with our first simulations [1], carried out on crystalline aggregates (constructed as superimpositions of random layers of columnar grains), a significant improvement is observed in the current full field 3-D predictions. This improvement is attributed to the more realistic 3-D mapping of the incipient microstructure, where both percolation and damage to the TiC phase are taken into account.

For each phase the computed average local stress  $\langle \sigma_{22} \rangle$  versus the applied strain  $E_{22}$  are represented by dotted

Table 3  
Set of parameters identified for molybdenum by Cédât et al. [1].

$\tau_0$	$a^{\text{su}} = a^{\text{su}}$	$\rho_0$	$g_{c0}$	$E_{gc}$	$D_{\text{grain}}$	$\tau_R$	$\dot{\gamma}_0$	$\Delta \hat{G}_0$	$p$	$q$
125 MPa	0.01	$10^{-11} \text{ m}^{-2}$	14 nm	$2.17 \times 10^{-2} \text{ eV}$	3 $\mu\text{m}$	498 MPa	$10^{-1}$	1.1 eV	0.2	1.5

lines. The molybdenum curve presents a perfect plastic behavior, whereas TiC shows a nonlinear behavior for  $0.5\% \leq E_{22} \leq 1.3\%$ , followed by a maximum, then a decrease. The perfect plastic behavior of the matrix corresponds to  $\langle \sigma_{22} \rangle = 590$  MPa (close to the behavior of pure metal Mo). The matrix yield stress is about 550 MPa and the constant stress corresponding to the plateau is equal to  $\Sigma_{22} = 620$  MPa up to  $E_{22} = 0.15$ . The nonlinear TiC curve corresponds to a decrease in the effective elastic modulus induced by damage.

The computed maps (Fig. 6) represent the evolution of the distribution of local strain  $\epsilon_{22}$  in the grains of Mo and TiC and of damage within the TiC particles. The local strain ( $\epsilon_{22}$ ) distribution is homogeneous in TiC grains and heterogeneous in large molybdenum grains. In TiC the damage parameter  $D(t)$  (introduced in Eqs. (10)–(12)) increases with applied deformation and locally reaches 1 for an applied strain  $E_{22} \cong 10\%$ . The value  $D = 1$  corresponds to rupture of the particles.

According to our numerical results we can propose the following scheme for damage. During stage I (the elastic stage) the TiC skeleton supports most of the deformation. At the end of stage I and up to a compression strain rate of 3% (stage II) some bridges of TiC (normal to the compression axes) are submitted to local tensile stress. As soon as the critical stress criterion (Eq. (10)) is breached some bridges between TiC particles are damaged. During stage II the damage parameter  $D$  increases, reaching 1 (rupture of the bridge) for  $E_{22} \cong 10\%$ . In stage III the composite behaves as a matrix with large disconnected particles.

5.2. Composite results for high temperatures

The numerical simulation and the corresponding experimental curves for high temperatures are given in Fig. 7.

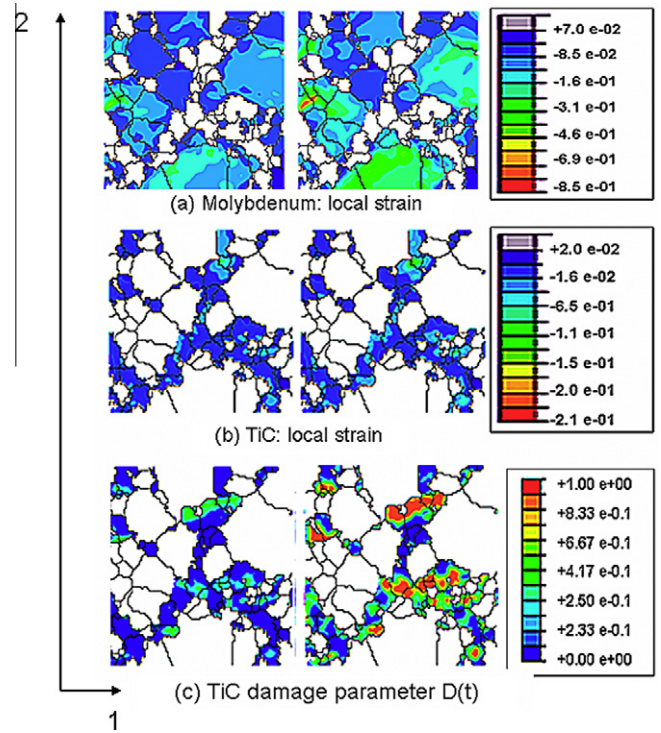


Fig. 6. Local strain  $\epsilon_{22}$  and damage evolution under two applied strains  $E = E_{22} = -0.03$  and  $E = E_{22} = -0.1$  at room temperature (the  $\vec{2}$  axis corresponds to the compression axis). (a) Molybdenum phase; (b) TiC phase; (c) damage parameter.

A comparison between the curves for the composite (Fig. 7a) and pure molybdenum (Fig. 7b) reveals, for an applied strain  $E_{22} = -0.09$ , a large increase in the macroscopic yield stress from 600 to 1450 MPa.

Fig. 7a shows, for  $E_{22} = -0.09$ , good agreement between the numerical and experimental results. The difference  $\Delta\Sigma_{22}$

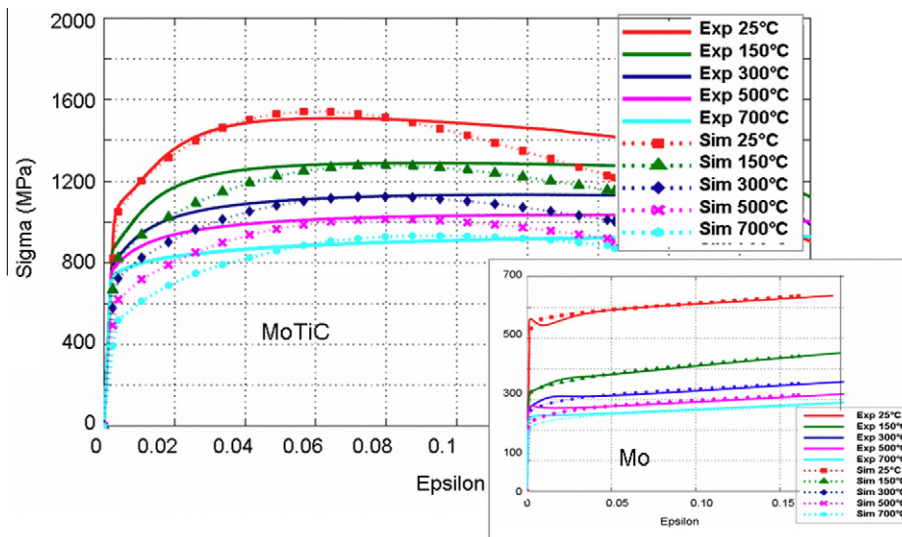


Fig. 7. Experimental and numerical stress–strain curves on a 3-D numerical model and a real polycrystalline aggregate of the composite for five temperatures. Experimental and numerical stress–strain curves on molybdenum are given in the inset.

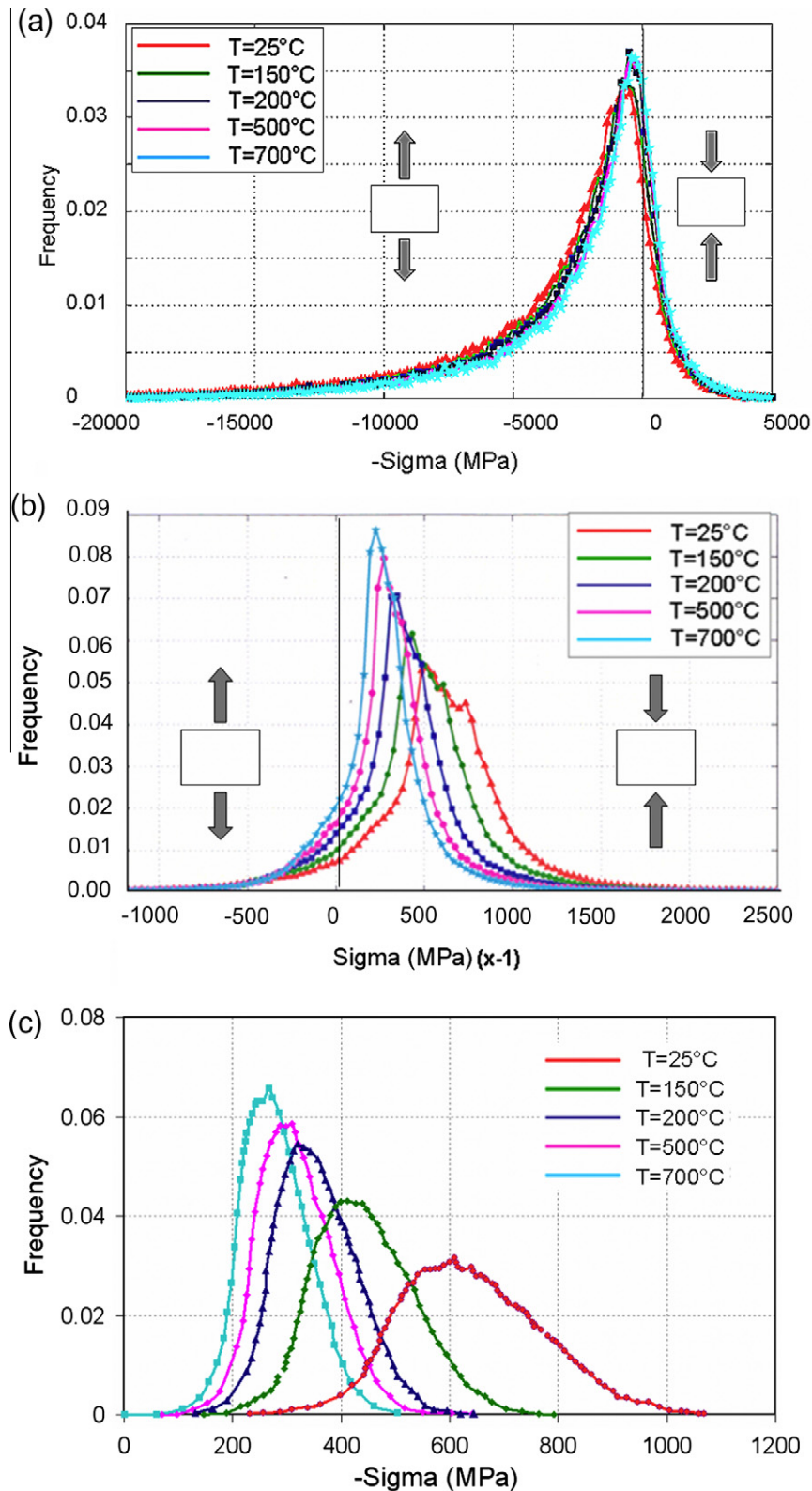


Fig. 8. Distribution of the uniaxial stress  $\sigma = \sigma_{22}$  for  $E_{22} = -0.09$ . (a) TiC phase; (b) molybdenum matrix; (c) pure molybdenum.

between the macroscopic experimental stress is less than 10 MPa. For small strains the agreement is only qualitative.

For the composite the small differences between the experimental results and simulation observed at the very begin-

ning of the plastic stage arise from the material parameters determined for pure molybdenum. For pure molybdenum the simulated yield stresses are lower than the experimental ones (Fig. 7b). The material parameters for pure molybdenum

(Tables 3 and 4) were identified, for  $E_{22} \geq 0.2\%$ , in simplified stress–strain curves. Accurate identification would need a higher number of material parameters. In addition, the damage may be considered much too simple. In stage II the average computed effective elastic modulus of the TiC bridges decreases less than is actually observed.

The computed distributions of internal stress  $\sigma_{22}$  for TiC ( $\sigma_{22}^{\text{TiC}}$ ) and Mo ( $\sigma_{22}^{\text{Mo}}$ ) are given in Fig. 8a and b. In order to understand the composite phase behavior the distribution  $\sigma_{22}^{\text{Mo}}$  for a pure molybdenum aggregate is reported in Fig. 8c.

Whatever the temperature, the TiC behavior being assumed to be elastic or brittle, the distribution  $\sigma_{22}^{\text{TiC}}$  is independent of the matrix behavior. In contrast, in the Mo matrix the distribution  $\sigma_{22}^{\text{Mo}}$  depends on both temperature and TiC behavior.

### 5.2.1. Molybdenum matrix

A comparison of the distributions  $\sigma_{22}^{\text{Mo}}$  (Mo matrix) and  $\sigma_{22}^{\text{Mo}}$  (pure Mo) for  $E_{22} = -0.09$  raises several important points.

- The  $\sigma_{22}^{\text{Mo}}$  distributions show high background noise and wider distributions than  $\sigma_{22}^{\text{Mo}}$ . It should be noted that some points in the Mo matrix are actually in traction. At these points the stress values can reach 500 MPa and can lead to damage to the matrix.
- For low temperatures the  $\sigma_{22}^{\text{Mo}}$  distribution curves present an asymmetry shape which disappears with increasing temperature. Our computation reveals that at 25 °C, 150 °C and 300 °C molybdenum grains close to inter-phase boundaries show very high internal stresses ( $\sigma_{22}^{\text{Mo}} \leq -500$  MPa).
- The average values  $\langle \sigma_{22}^{\text{Mo}} \rangle$  and  $\langle \sigma_{22}^{\text{Mo}} \rangle$  are very close and show the same evolution with temperature. These values correspond to the macroscopic stress of pure molybdenum compression curves.

### 5.2.2. TiC carbide

Although for  $E_{22} = -0.09$  some TiC bridges are broken ( $D(t) = 1$ ), a small part ( $\sim 15\%$ ) of the TiC phase is still submitted to local tensile stresses greater than the critical stress ( $\sigma_c \geq 250$  MPa). Damage evolution then slows down in stage III. The TiC skeleton presents a number of micro-cracks and the composite is reduced to a Mo matrix with large TiC inclusions. As a result the composite hardening slope plateaus, before becoming negative. At high temperatures evolution of the damage parameter with applied deformation is slowed down compared with low temperatures, leading to an increase of the size of the plateau.

Damage is represented by decay of the effective elastic modulus in some elements of the TiC mesh as soon as the critical stress criterion is satisfied. The square elements of the mesh are more representative of small holes than actual thin micro-cracks. The increasing number of “holes” in TiC is sufficient to explain the weak negative slope of the simulated stress–strain curves for large strains.

## 6. Conclusions

Understanding the mechanical behavior of a two-phase Mo–TiC<sub>30 vol.%</sub> metal–ceramic composite over a wide temperature range requires simultaneous experimental and numerical studies. The first difficulty is to work on a realistic representation of the material, then to take into account damage to the brittle phase and its effect on the ductile phase. The composite studied presents small grains and a brittle phase with percolation, the crystalline orientation of which is not easily observable. Mechanical polishing and EBSD measurements cannot be used in this case and aggregates built from random layers of grains lead to incorrect results. Consequently, a dual beam FIB-SEM was used to characterize and reconstruct a real 3-D polycrystalline two-phase Mo–TiC<sub>30 vol.%</sub> metal–ceramic composite aggregate layer by layer. Implementation of damage to the brittle phase on the scale of the grain is required and provides good results for the microscopic stress–strain fields when applied to this 3-D aggregate. The TiC damage criterion is described in terms of cumulative decay in the elastic stiffness of this phase as a function of straining. Very good agreement with the experimental curves is observed at 25 °C. The stage III behavior is accurately described for any temperature.

The proposed 3-D aggregate and the corresponding two-phase polycrystal model can be used to forecast the behavior of any related metal–ceramic or metal–metal composite at different temperatures, just by changes in the matrix and particles parameters.

## Acknowledgements

The microstructure of the starting composite was characterized at the Max Planck Institute Düsseldorf. The authors are very grateful to Prof. S. Zaefner for his kind and helpful discussions. The Mo–TiC composite studied was elaborated at the Commissariat à l’Energie Atomique. The authors thank Drs M. Le Flem and J.L. Bechade for giving us the material and for financial help with the tomography experiments. The authors are grateful to Prof. J.H. Schmitt (ECP) for stimulating and helpful discussions.

## References

- [1] Cédât D, Libert M, Le Flem M, Fandeur O, Rey C, Clavel M, et al. Int J Refract Met Hard Mater 2009;27:267–73.
- [2] Eitmayer P, Kolaska H. In: Bildstein H, Ortner HM, editors. 12th Plansee seminar; 1989. p. 771–801.
- [3] Le Flem M, Allemend A, Urvoy S, Cédât D, Rey C. J Nucl Mater 2008;380:85–92.
- [4] Cédât D, Rey C, Clavel M, Schmitt JH, Le Flem M, Allemend A. J Nucl Mater 2009;385:533–7.
- [5] Uchic MD, Groeber M, Dimiduk DM, Simmons JP. Scripta Mater 2006;55:23–8.
- [6] Zaefner S. Mater Sci Forum 2005;495-497:3–12.
- [7] Bastos A, Zaefner S, Raabe D. J Micros 2008;230:487–98.
- [8] Konrad J, Zaefner S, Raabe S. Acta Mater 2006;54:1369–80.

- [9] Larson BC, Yang W, Ice GE, Bhai JD, Tischler JZ. *Nature* 2002;425:887–90.
- [10] Yang W, Larson BC, Pharr GM, Ice GE, Tischler JZ. *MRS Symp Proc* 2003;779:W5.34.1.
- [11] Zaafarani N, Raabe D, Singh RN, Roters F, Zaefferer S. *Acta Mater* 2006;54:1863–76.
- [12] Zaefferer S, Wright SI, Raabe D. *Metal Mater Trans A* 2008;39A:374–89.
- [13] Cédât D. PhD thesis, Ecole Centrale Paris, France; 2008.
- [14] Libert M, Rey C, Vincent L, Marini B. *Int J Solids Struct* 2011;48:2196–208.
- [15] Peirce D, Asaro RJ, Needleman A. *Acta Metall* 1983;31:1951–76.
- [16] Teodosiu C, Raphanel JL, Tabourot L. Large plastic deformation. Proceedings of the international seminar MECAMAT '91; 1991. p. 153–68.
- [17] Eriau P, Rey C. *Int J Plast* 2004;20:1763–88.
- [18] Ma A, Roters F, Raabe D. *Acta Materialia* 2006;54:2169–79.
- [19] Libert M. PhD thesis. Ecole Centrale Paris, France; 2007.
- [20] Roters F, Eisenlohr P, Hantcherli L, Tjahjanto D, Bieler TR, Raabe D. *Acta Mater* 2010;58:1152–211.
- [21] Kubin LP, Louchet F, Vesely D. *Philos Mag A* 1978;38:205–21.
- [22] Rauch E. *Key Eng Mater* 1994;97/98:371–6.
- [23] Tabourot L, Fivel M, Rauch E. *Mater Sci Eng A* 1997;234/235:639–42.
- [24] Kocks UF, Argon AS, Ashby MF. *Prog Mater Sci* 1976;19.
- [25] Franciosi P. *Acta Metall* 1983;31:1331–42.
- [26] Estrin Y, Mecking H. *Acta Metall* 1984;32:57–70.
- [27] Ma A, Roters F, Raabe D. *Acta Mater* 2006;54:2181–94.
- [28] Sadowski T, Samborski S. *Comput Mater Sci* 2003;28:512–7.